

# Galaxy clustering using photometric redshifts

A. M. Soltan<sup>★</sup> and M. J. Chodorowski<sup>★</sup>

*Nicolaus Copernicus Astronomical Centre, Bartycka 18, PL-00-716 Warsaw, Poland*

Accepted 2015 July 21. Received 2015 June 16; in original form 2014 November 20

## ABSTRACT

We investigate the evolution of the galaxy two-point correlation function (CF) over a wide redshift range,  $0.2 < z \lesssim 3$ . For the first time, the systematic analysis covers the redshifts above 1–1.5. The catalogue of  $\sim 250\,000$  galaxies with  $i^+ < 25$  and known photometric redshifts in the Subaru Deep field is used. The galaxies are divided into three luminosity classes and several distance/redshift bins. First, the 2D CF is determined for each luminosity class and distance bin. Calculations are based on the quantitative differences between the surface distributions of galaxy pairs with comparable and distinctly different photometric redshifts. The power-law approximation for the CF is used. A limited accuracy of photometric redshifts as compared to the spectroscopic ones has been examined and taken into account. Then, the 3D functions for all the selected luminosities and distance are calculated. The power-law parameters of the CF, the slope and the correlation length are determined. Both parameters do not show strong variations over the whole investigated redshift range. The slope of the luminous galaxies appears to be consistently steeper than that for the fainter ones. The linear bias factor,  $b(z)$ , grows systematically with redshift; assuming the local normalization  $b(0) \approx 1.1\text{--}1.2$ , the bias reaches 3–3.5 at the high-redshift limit.

**Key words:** galaxies: distances and redshifts – galaxies: statistics – galaxies: structure.

## 1 INTRODUCTION

Growth of galaxy structures provides an essential information on the evolution of the dark matter distribution (Marulli et al. 2013, and references therein). Observations of the large-scale structures (LSSs) would – possibly – give insight also into the very nature of dark energy (e.g. Jenkins et al. 1998; Jennings, Baugh & Pascoli 2011; Huterer et al. 2015). Gravitationally dominating dark matter induces growth of the density fluctuations that eventually lead to the formation of galaxies. From that moment on, the large-scale matter distribution generated in the computer simulations becomes, at least potentially, subject to the observational constraints.

However, distinctly different physical properties of the collisionless dark matter and the visible, baryonic matter make the interplay between those constituents intricate. Flows of baryonic matter towards gravitational wells created by concentrations of the dark matter involve complex processes of gas accretion, shock heating and radiative cooling. In effect, the observable galaxy structures do not follow exactly the dark matter distribution. The relationship between the density fluctuations of the galaxies and dark matter was formulated on statistical grounds by Kaiser (1984). The amplitude ratio of these fluctuations, known as the galaxy bias, is roughly linear, although it depends on the smoothing scale (Mo & White 1996). The bias is also a function of time (e.g. Fry 1996). More-

over, the galaxy clustering depends on galaxy luminosity, mass, colour and other parameters. In the local Universe, these relationships have been extensively investigated (e.g. Coupon et al. 2012, see also Marulli et al. 2013, for the comprehensive reference list).

Complex dark matter structures generated by the gravitational instability revealed in the cosmological simulations combined with the obscure nature of the dark matter itself open a space for models that describe the distribution of luminous matter with the dark one (e.g. Berlind & Weinberg 2002; Papageorgiou et al. 2012). The study of the luminous–dark matter relationship incorporates two separate issues: adequate statistical description of the galaxy distribution and comprehensive cosmological simulations of the dark matter. Both determined over a wide redshift range. In the present paper, we concentrate on the galaxy distribution. This question has been investigated extensively for a long time and in recent years gained momentum mostly as a result of massive automated galaxy surveys. Although many characteristics of the galaxy clustering are precisely measured at selected magnitudes and/or redshifts, the evolution of the clustering over a wide redshift range is still not well determined. In the present paper, we pursue this question, i.e. to what extent the observational data constrain parameters of the cosmic evolution of the galaxy clustering over the whole observable cosmic time.

In most cases, questions related to the galaxy clustering are adequately addressed using the correlation functions (CFs). Usually, the observed function is satisfactorily represented by a power law with two fitted parameters – the correlation length and slope. Only the

<sup>★</sup> E-mail: [soltan@camk.edu.pl](mailto:soltan@camk.edu.pl) (AMS); [michal@camk.edu.pl](mailto:michal@camk.edu.pl) (MJC)

high-quality statistical material allows for more detailed study (e.g. Baugh 1996; Norberg et al. 2002; Martinez-Manso et al. 2015). Here, we apply the power-law model for two reasons. First, the present data do not allow for the more refined analysis, and second, our method works efficiently using this approximation. Additionally, we believe that a question of the clustering evolution is still adequately addressed by the search for variations with time of the power-law parameters. A large number of investigations in the recent years examined how the shape of the galaxy CF depends on the overall galactic parameters such as stellar mass, luminosity, type, colour or star formation rate. In the local Universe and at low to moderate redshifts, all these studies indicate that the amplitude of the CF increases with luminosity (e.g. Norberg et al. 2002; Pollo et al. 2006; Coil et al. 2006; Li et al. 2006; Wake et al. 2011; Zehavi et al. 2011; Marulli et al. 2013), although strength of this dependence is disputable (Meneux et al. 2009), or limited to specific types of galaxies (e.g. Lin et al. 2012; Mostek et al. 2013). On the other hand, several studies indicate little or no dependence of the correlation slope on galaxy parameters (e.g. Norberg et al. 2002; Coil et al. 2006; Marulli et al. 2013), but see Pollo et al. (2006).

If no information on the galaxy radial distance is available, the amplitude of spatial correlations is derived from the 2D CF. Efficiency of this approach is limited to relatively shallow galaxy samples. This is because in the deep galaxy surveys the correlation signal is diluted by a large number of random coincidences. Galaxy catalogues with redshifts offer a natural method to eliminate most of the random coincidences, what substantially improves the signal to noise (S/N) ratio. Unfortunately, acquisition of the spectroscopic redshifts is time consuming and restricted to relatively bright objects.

The photometric redshifts, as compared to the spectroscopic ones, are substantially less accurate distance indicators. Nevertheless, they provide at least raw estimate of the galaxy position. Thus, photometric redshifts could be used to identify and extract evident random pairs, and to increase in this way the S/N ratio of the correlation amplitude measurement. The photometric redshifts were successfully used in the past for the investigations of the angular clustering (Heinis et al. 2007; McCracken et al. 2008; Wake et al. 2011), and the spatial clustering (Arnalte-Mur et al. 2014; Bielby et al. 2014). In the present paper, we apply a different technique to obtain the galaxy CF for a wide range of redshifts, not covered by previous investigations. We use the 2 deg<sup>2</sup> COSMOS photometric redshift catalogue by Ilbert et al. (2009) available through the Web site of IPAC/IRSA.

According to a standard procedure, to determine the 2D CF one generates a large set of randomly distributed points. Properly normalized numbers of galaxy-random point pairs is then used as a reference distribution of pair separations representing a random galaxy population. A comparison of the physical galaxy-galaxy pairs with the galaxy-random point pairs allows one to assess fluctuations of the galaxy distribution and eventually to calculate the correlation signal. The efficiency of this method is highly sensitive to the interference with the cosmic signal of various selection effects related to the data processing. For instance, even a minute variations in the catalogue depth or the image quality result in fluctuations of the surface density of objects, that could be easily misidentified with the galaxy clustering. To minimize these kind of confusions, the ‘random’ points should be distributed in such a way as to mimic all the inhomogeneities of the non-cosmic origin. The performance of this widely applied procedure depends on how precisely such mock catalogues are free from all the observational biases.

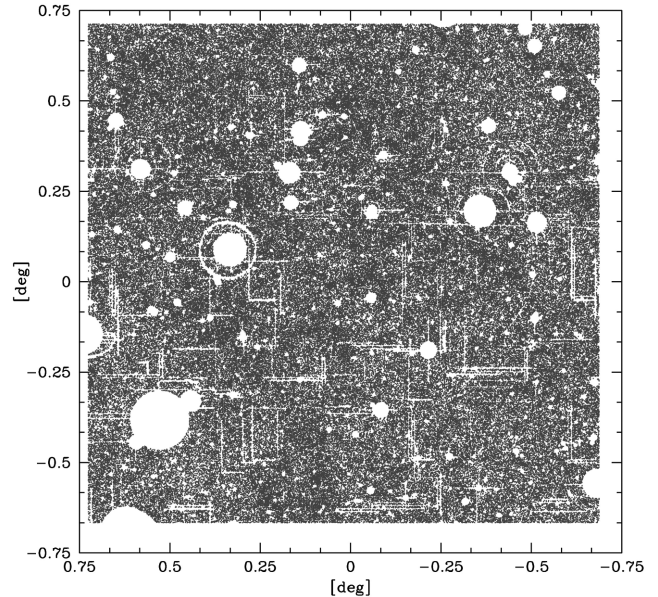


**Figure 1.** Distribution of  $\sim 250\,000$  COSMOS galaxies. An uneven data coverage affects the galaxy correlation analysis.

To reduce the instrumental bias, we apply here a different attitude. We assess the number of galaxy pairs expected for the random distribution by means of the galaxy-galaxy pairs with sufficiently different photometric redshifts that effectively exclude physical connection. Distribution of such pairs incorporates most signatures associated with the data bias and processing, while it is free from the physical clustering signal.

The organization of the paper is as follows. In the next section, we give a short description of the COSMOS photometric redshift catalogue. In Section 3, we describe the details of the present method to calculate the 2D CF, derive the relevant formulae and present results of these calculations. Formulae applied to determine the 3D CFs for different luminosities and over a several redshift bins are given in Section 4. Also statistical properties of the photometric redshift measurements are described in this section. The evolution of bias in the linear model, and short comparison of our measurements on the CF evolution with the selected previous results is presented in Section 5. Strong and weak points of our method are summarized here.

In the paper, we consistently parametrize the COSMOS catalogue data and results of the investigation using the comoving distances alongside the redshift. To convert redshifts to the comoving distances, we use the flat cosmological model with  $H_0 = 70 \text{ km s}^{-1} \text{ Mpc}^{-1}$ ,  $\Omega_{m,0} = 0.3$  and  $\Omega_{\Lambda,0} = 0.7$ .

## 2 THE DATA

The COSMOS photometric redshift catalogue is presented in detail by Ilbert et al. (2009). Here, we give only the information relevant to the present investigation. The catalogue contains 38 5065 objects in the deep Subaru Area, of which almost 252 000 have been classified as galaxies brighter than  $i_{AB}^+ = 25$ . The galaxies are distributed within a square of 84 arcmin a side centred at  $\alpha_c = 150^{\circ}1$  and  $\delta_c = 2^{\circ}2$  (Taniguchi et al. 2007). However, the data coverage is non-uniform on various angular scales. In Fig. 1, the distribution of all the galaxies is shown. One can see a large number of masked areas of poor image quality (mostly saturated star images and CCD related problems).

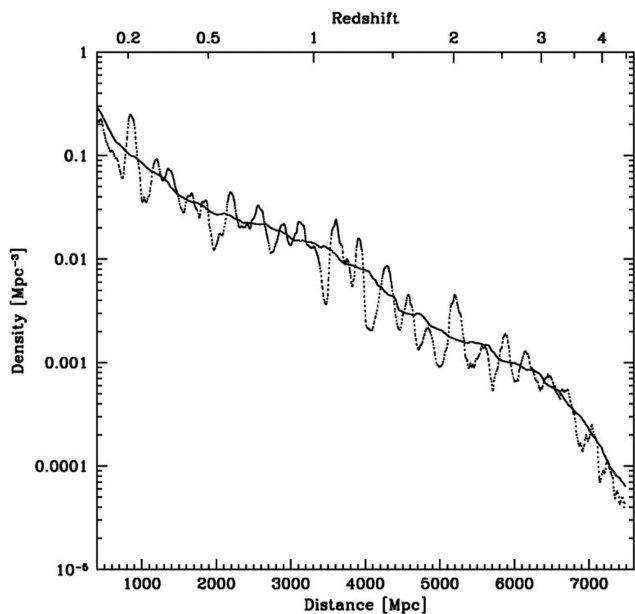


**Figure 2.** The spatial density of the COSMOS galaxies as a function of the comoving distance (bottom abscissa) or redshift (top abscissa). Highly fluctuating (dotted) curve represents the moving average calculated within  $\pm 50$  Mpc, while the smoother one (solid) – within  $\pm 500$  Mpc.

To measure the photometric redshifts *Le Phare*<sup>1</sup> algorithm (Arnouts & Ilbert 2011) was applied using 30 filters that cover UV, optical and NIR. According to Ilbert et al. (2009), the photo- $z$  accuracy depends on galaxy redshift and magnitude, and it is suitably characterized by  $\sigma_{\Delta z/(1+z_s)}$  defined as  $1.48 \times \text{median}(|z_p - z_s|/(1+z_s))$ , where  $z_p$  and  $z_s$  denote photometric and spectroscopic redshift, respectively. For  $i_{AB}^+ < 22.5$  a dispersion  $\sigma_{\Delta z/(1+z_s)} = 0.007$ , while for  $i_{AB}^+ < 24$  and  $z < 1.25$ ,  $\sigma_{\Delta z/(1+z_s)} = 0.012$ . At fainter magnitudes, the estimates are less accurate, e.g. for  $i_{AB}^+ \sim 24$  and  $z \sim 2$ ,  $\sigma_{\Delta z/(1+z_s)} = 0.06$ .

Although the distribution of differences  $(z_p - z_s)/(1+z_s)$  is roughly fitted by a Gaussian function, the median statistics in the  $\sigma_{\Delta z/(1+z_s)}$  definition above indicates that gross errors affect occasionally the  $z_p$  estimates. Ilbert et al. (2009) define a ‘catastrophic failures’ of the  $z_p$  estimate if  $|z_p - z_s|/(1+z_s) > 0.15$ . In the case of bright galaxies ( $i_{AB}^+ < 22.5$ ), the fraction of catastrophic failures amounts to 0.7 per cent. It rises however, to 20 per cent for galaxies at  $1.5 < z_s < 3$ . The median apparent magnitude of those galaxies  $i_{AB}^+ \sim 24$ .

The distribution of  $z_p$  over  $z_s$  exhibits also some peculiarities that are not depicted by  $\sigma_{\Delta z/(1+z_s)}$ . The  $z_p - z_s$  differences are correlated with  $z_s$  over scales comparable and larger than the quoted above dispersion  $\sigma_{\Delta z/(1+z_s)}$ . In the right-hand panel of fig. 10 in Ilbert et al. (2009), the distribution of  $z_p$  versus  $z_s$  exhibits systematic, to some extent coherent variations around the line  $z_p = z_s$ , indicating the non-random, large-scale deviations between  $z_p$  and  $z_s$ . The effect of the non-random character of  $z_p$  deviations from the spectroscopic data is graphically demonstrated in Fig. 2, where we plot a moving average density of galaxies in the COSMOS catalogue. We count galaxies within 50 Mpc of the radial distance for each object in the catalogue. The  $z_p$  redshifts are used in the calculations. Number of neighbours

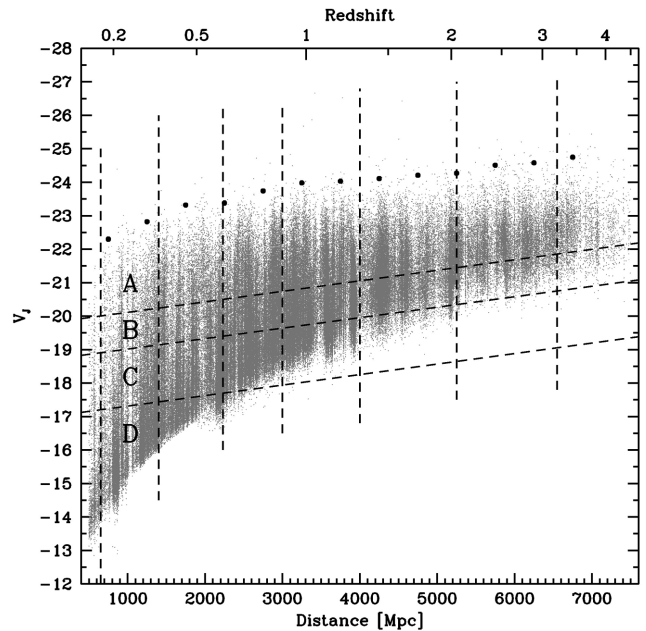


**Figure 3.** The distribution of galaxies in the absolute  $V_J$  magnitude – comoving distance plane. Inclined dashed lines indicate luminosity sub-samples A–D, while the vertical lines define distance bins used in the calculations. Full dots – see text.

is then used to assess the local spatial concentration of galaxies as a function of distance. Apparent quasi-periodic oscillations around the average galaxy density in the distance range  $\sim 2000$  through  $\sim 7000$  Mpc with the characteristic length of  $\sim 330$  Mpc demonstrate the large-scale inhomogeneities in the  $z_p$  measurements.

Both the  $z_p$  inaccuracies and the sky coverage discontinuities introduce multiple biases in the COSMOS galaxy data that distort the actual spatial structures. Although it is feasible to construct the mask that would eliminate (all ?) the area not covered by the COSMOS catalogue, the remaining surface non-uniformities potentially present in the data would persist. In the next section, we present a practical method how to isolate the real clustering signal from all the non-cosmic effects.

The sample spans a wide range of absolute magnitudes. In Fig. 3, the absolute  $V_J$  magnitudes (Ilbert et al. 2009) are plotted against the distance. Apart from the clear effects introduced by the  $z_p$  distortions, an inclination of the high-luminosity envelope defines a rate of the average galaxy luminosity evolution. Black dots in Fig. 3 show the magnitudes of 10th ranked galaxy in 500 Mpc bins between 500 and 7000 Mpc. Although in the course of the cosmic evolution galaxy luminosities are subject to more complex variations, we adopt here this relationship as the luminosity evolution of the general galaxy population. We divide the data into absolute magnitude classes using lines of fixed slope roughly consistent with the slope of the  $V_J(10)$  – distance relationship (see Fig. 3). The dashed lines in the figure define four luminosity sub-samples. The samples A–C contain  $\sim 70000$  galaxies each, while the sample D – around half of this amount. Because the D sample is limited to redshifts smaller than 0.5, the present analysis of the clustering evolution concentrates on samples A–C. Although the rate of the luminosity evolution adopted here is linear in the comoving distance, it is in good agreement with the evolution model (linear in redshift) adopted by Marulli et al. (2013) in the redshift range of 0.5–1.1.

Moving to larger distances all the galaxy sub-samples become increasingly incomplete (Fig. 2 for the whole data, and Fig 10 for

<sup>1</sup> [www.cfht.hawaii.edu/~arnouts/LEPHARE/DOWNLOAD/lephare\\_doc.pdf](http://www.cfht.hawaii.edu/~arnouts/LEPHARE/DOWNLOAD/lephare_doc.pdf)

the class A). This effect should not coerce the measurements of the CF if the magnitude selection at a given distance is uncorrelated with the local galaxy space density, and this is assumed in the subsequent calculations.

### 3 2D CORRELATION FUNCTIONS

We take the photometric redshifts,  $z_p$ , as a working estimate of the comoving distances for all the galaxies. This is a legitimate assumption for the majority of galaxies. According to Ilbert et al. (2009), only a (small) fraction of  $z_p$  differs from  $z_s$  by more than  $0.15 \cdot (1 + z_s)$ . Nevertheless, in the present derivation we explicitly take into account a questionable nature of the individual distance estimate. This is because even a modest fraction of catastrophic errors affects the present analysis (see below).

Clearly, the distance estimates based on  $z_p$  are too coarse to measure directly the spatial clustering. Nevertheless, the  $z_p$  data are valuable in measurements of the galaxy clustering at different distances using the 2D CF. Let us to consider the expected distribution of galaxies around the galaxy selected at a distance  $d = d(z_p)$ . The expected number of galaxies within a solid angle  $\Delta\omega$  at the angular distance  $\theta$  from the selected galaxy,  $N(\theta)$ , is described by the 2D CF  $w(\theta | d)$ :

$$N(\theta) = \Delta\omega [n_o \cdot w(\theta | d) + n_o], \quad (1)$$

where  $n_o$  is the galaxy surface density expected in the absence of cosmic clustering. For the perfect data,  $n_o$  is equal to the mean galaxy surface density. However, the present observational material reveals numerous defects that interfere with the sky fluctuations. In effect, the local ‘background’ galaxy density,  $n_o$ , is not constant but depends on the position of selected galaxy and the separation  $\theta$ .

For the data spanning a large distance range as in the case of the COSMOS catalogue, equation (1) is of a limited use because the excess of neighbours,  $\delta N(\theta) = N(\theta) - \Delta\omega \cdot n_o$ , even at small separations  $\theta$ , is tiny as compared to  $\Delta\omega \cdot n_o$ . To improve the S/N ratio, which is of the order of  $\delta N(\theta)/\sqrt{N(\theta)}$ , we divide the whole galaxy sample into six distance bins between 650 and 6550 Mpc. The radial depth of each bin is larger than 750 Mpc. Thus, it is also much larger than the maximum distance at which the CF differs from 0.

Calculating the surface correlations of galaxies within a selected bin, we split the whole galaxy population into two classes. Class I contains galaxies located in the bin of the selected galaxy, while the class II contains all the galaxies in other bins. The expected average excess of galaxies,  $N_I(\theta)$  or the surface density profile,  $n_I(\theta)$ , of class I galaxies in the vicinity of the galaxy drawn from the same distance bin is described by the CF  $w_I(\theta)$ :

$$\frac{N_I(\theta)}{\Delta\omega} = n_I(\theta) = n_{I0} \cdot w_I(\theta) + n_{I0}, \quad (2)$$

where  $n_{I0}$  is the class I galaxy surface density expected for the non-clustered case. It is subject to various observational constraints and it may vary alike  $n_o$ . We now assume a power law for the  $w_I(\theta)$  function separately for each bin:

$$w_I(\theta) = w_i \theta^{\zeta_i}, \quad i = 1, \dots, 6. \quad (3)$$

In the absence of all the effects involved in the data acquisition that hamper the genuine sky distribution of galaxies, one could use directly equations (2) and (3) to determine the amplitude,  $w_i$  and slope,  $\zeta_i$ . However, in the real data the ‘average’ galaxy density,  $n_{I0}$ , is not well defined. One way to eliminate effects of the  $n_{I0}$  fluctuations is to use the surface distribution of class II galaxies,

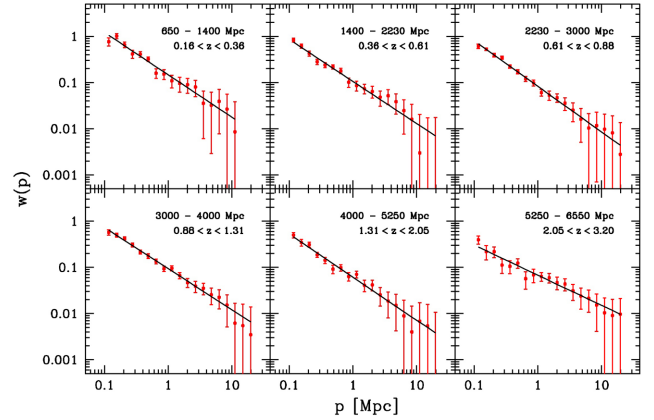


**Figure 4.** The surface correlation functions for the luminous galaxies (sample A) in the six distance bins (labelled in the bottom left corner), the distance/redshifts boundaries are indicated in the top right corner. The data points,  $1\sigma$  error bars and the power-law least-squares solutions of equation (4) are shown.

$n_{II0}$ . We assume that intruding (non-cosmic) factors that affect the surface distribution of class I galaxies modify also distribution of class II galaxies. Although a response of both galaxy population to various effects may not be identical, we assume that the ratio  $\eta_i = n_{I0}/n_{II0}$  is much more immune to observational biases than  $n_{I0}$  and  $n_{II0}$  separately. Thus, dividing equation (2) by  $n_{II0}$ , we get the numerically tractable equations:

$$\frac{N_I(\theta)}{N_{II}(\theta)} = \eta_i w_i \theta^{\zeta_i} + \eta_i, \quad (4)$$

where  $N_{II}(\theta) = \Delta\omega \cdot n_{II0}$  is the average number of class II galaxies at the distance  $\theta$  from the randomly chosen galaxy of class I. As an estimator of  $N_I(\theta)$  and  $N_{II}(\theta)$  for the given distance bin we use the total numbers of the class I galaxy pairs and the class I–class II pairs, respectively, both summed over the entire field.

To assess the power-law parameters of the angular CF, the present method applies the pair count ratio  $n_{I0}/n_{II0}$  rather than just the pair counts  $n_{I0}$ . This scheme deals simultaneously with two questions. First, it accounts in a simple way for all the masked out areas. Second, if there are some unrecognized systematic effects that perturb the surface galaxy distribution, they are absorbed by the  $\eta_i$  parameter while the pure clustering signal is represented by the power law.

The parameters  $w_i$ ,  $\zeta_i$  and  $\eta_i$  for each distance bin  $i$  are obtained as the iterative least-squares solution of equation (4). Two first parameters,  $w_i$  and  $\zeta_i$ , define the 2D CFs. The results for the luminosity sample A are shown in Fig. 4. To ease the comparisons of the correlation parameters in the different bins, and to indicate what linear distances are involved in the calculations of the space CF (see below), we plot the data as a function of the transverse comoving distance,  $p$ , rather than the angular separation, with  $p = \theta \cdot R_i$ , where  $R_i$  denotes the distance to the centre of the  $i$ th bin. In all the distance bins, except for the nearest one, the galaxy pairs are counted in 19 separation zones in the range of  $0.1 < p < 22.6$  Mpc. In the nearest distance bin (650–1400 Mpc) the range of separations is reduced to  $0.1 < p < 10.0$  Mpc due to the small angular size of the COSMOS field.

The parameters  $w_i$  depend on the actual 3D clustering amplitude and on the surface density of galaxies in the consecutive distance bins. To assess the spatial clustering, one requires the information on the spatial density of galaxies in the each bin, and this question is

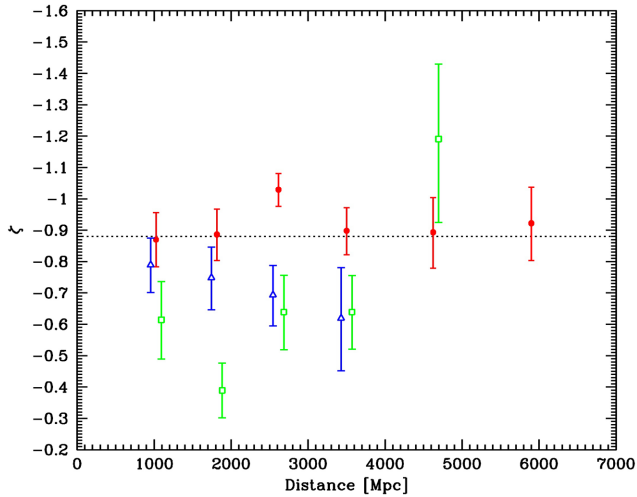


**Figure 5.** The 2D correlation function slopes: full points – luminosity class A, open circles – class B, triangles – class C.

discussed below. The CF slopes,  $\zeta_i$ , are not greatly affected by the bin limits. In Fig. 5, variations of the correlations slopes as a function of distance are shown for galaxies in three luminosity samples. The error bars indicate 68 per cent confidence levels assuming one interesting parameter (Avni 1976). Large  $\zeta_i$  uncertainties in the samples B and C make any definite account on the slope variations problematic. Nevertheless, two conclusions seem to be relatively well established. First, no obvious trend of slope changes with the distance is present in any of the galaxy luminosity samples. Second, the slope for the most luminous galaxies (sample A) is generally steeper than that for the remaining ones. The detailed interpretation of the present results on CF slope is discussed jointly with the amplitude of the spatial CF in Section 5.

#### 4 3D CORRELATION FUNCTIONS

We use the photometric redshifts solely to define wide distance bins, and not to examine individual galaxy pairs in 3D. The excess number of close pairs relative to that expected for the random distribution is clearly visible in each bin. The fine 2D correlation signal shows that the statistical characteristics of photometric redshifts are sufficient to determine the evolution of the CF slope over a wide range of cosmological epochs. To assess the amplitude of the space correlations at successive distances, one should deproject the corresponding surface CFs.

The space CF gives the number of excess galaxy pairs relative to the local average galaxy density. In the present investigation, the galaxy density varies between bins and also within each individual bin. However, these variations do not constrain the CF estimates. The galaxy excess given by the 2D CF is equal to the integral of the space 3D properly weighted by the space density of galaxies populating the selected distance bin. Below the deprojection procedure is described in detail.

A power law provides not only satisfactory approximation to the 2D CF, but also allows for a straightforward assessment of the spatial correlation parameters. Under the standard assumption of clustering isotropy and small angles approximation, the spatial CF is a power law with a slope  $\gamma = \zeta - 1$ . To retrieve the normalization of the spatial correlations from the 2D function, one needs the information on the radial distribution of the average galaxy density in the sample. In the present analysis, the galaxy concentration

varies systematically with the radial distance. We now derive the formulae relating the 3D CF to the 2D function and the varying galaxy density.

The 3D CF measures the local average excess of galaxies relative to the average density of galaxies. Let  $\Delta N_V(r)$  is the average excess of galaxies, i.e. the number of galaxies above the average within a volume  $\Delta V$  at a distance  $r$  from the randomly chosen galaxy. The CF  $\xi(r)$  is proportional to the number of excess objects:

$$\Delta N_V(r) = \Delta V \rho \xi(r), \quad (5)$$

where  $\rho$  denotes the average galaxy density. In the present data, the average galaxy density is strongly varying function of the distance  $R$  within each bin,  $\rho = \rho(R)$ . Using the power-law model for  $\xi$ :

$$\xi(r) = \left(\frac{r}{r_0}\right)^\gamma, \quad (6)$$

where  $r_0$  is the correlation length, one can integrate the galaxy excess (equation 5) along the line of sight at fixed transverse separation  $p$ :

$$\Delta N_A(p) = \Delta A G(\gamma) r_0^{-\gamma} \rho(R) p^\zeta, \quad (7)$$

where  $\Delta A$  is the surface area of volume  $\Delta V$  projected in the sky plane, and  $G(\gamma) = \Gamma(\frac{1}{2}) \Gamma(-\frac{\gamma}{2} - \frac{1}{2}) / \Gamma(-\frac{\gamma}{2})$  (Totsuji & Kihara 1969). In the actual calculations, the maximum radial separation of galaxy pairs is limited by the bin boundaries, what reduces the  $G(\gamma)$  factor. The amplitude of this effect depends on the radial distribution of the galaxy density (see Section 4.3). In the present case, the radial depth of the distance bin is non-negligible in comparison to the distance  $R$  itself. The counts of galaxy pairs are in fact performed within the fixed angular separation  $\theta$  rather than the  $p$ . Substituting  $p = \theta \cdot R$  and  $\Delta A = \Delta \omega \cdot R^2$  into equation (7) we get:

$$\Delta N_\omega(\theta) = \Delta \omega G(\gamma) r_0^{-\gamma} \rho(R) \theta^\zeta R^{\gamma+3}, \quad (8)$$

where the subscript  $\omega$  indicates that counts are collected within the solid angle  $\Delta \omega$ . Notice that here  $p$  and  $\theta$  are related to the varying distance  $R$  rather than to the bin centre  $R_i$ . The excess  $\Delta N_\omega(\theta)$  averaged over all the galaxies found in the selected distance bin is given by

$$\overline{\Delta N_{\omega_i}(\theta)} = \Delta \omega G(\gamma_i) r_{0i}^{-\gamma_i} \theta^{\zeta_i} \frac{\int dR R^{\gamma_i+5} \rho_i^2(R)}{\int dR R^2 \rho_i(R)}. \quad (9)$$

The index  $i$  specifies that only galaxies assigned to the  $i$ th distance bin are used to count the galaxy pairs, and  $\rho_i(R)$  is the average density of these galaxies at the distance  $R$ . The galaxy excess at the left-hand side of equation (9) is equal to that in equations (2) and (3) using the 2D correlations:

$$\overline{\Delta N_{\omega_i}(\theta)} = \Delta \omega n_{i0} w_i \theta^{\zeta_i}. \quad (10)$$

Here,  $n_{i0}$  denotes the observed average surface density of galaxies of the  $i$ th distance bin. The average radial density distribution,  $\rho_i(R)$ , in equation (9) is the actual distribution that might not be adequately described by the photometric redshift distribution. The question of statistical reconstruction of the spectroscopic redshift distribution based on the photometric redshifts is discussed in the next section.

We use the term ‘spectroscopic redshift’ to denote the perfect distance measure based on the Hubble expansion. The actual spectroscopic redshifts are neither sufficiently accurate, nor adequately represent the Hubble flow. In the present consideration, the statistical relationships between the redshift distributions is used to assess the average distribution of galaxy spatial density as a function of cosmological distance. Thus, small deviations between the ‘Hubble

flow redshifts’ and their spectroscopic counterparts are of no importance. One should note also that the photometric redshifts are used in the present calculations exclusively to define distance bins and not to compute galaxy separations in the radial direction. Thus, the construction of the 3D CF is not affected by the ‘redshift distortions’ that modify the separations between objects.

A question of the radial distribution of the average galaxy density,  $\rho(R)$ , deserves more comment. The transverse extension of the COSMOS field at distances 4000–6000 Mpc amounts to 100–150 Mpc (in comoving units), and even at large distances the survey area is smaller than typical LSSs. However, both the transverse survey size as well as the radial extension of the distance bins are distinctly larger than the galaxy pair separations used in the CF estimates (nearly all the correlation signal is limited to projected separations below 10 Mpc). Since the average density  $\rho(R)$  and the CF are determined using the same observational material, the small-scale fluctuations defined by the CF are measured ‘on top’ of the LSS potentially present in the data. From that point, it would be desirable to compare our results with the deep CF assessments in other fields.

#### 4.1 Modelling the photometric redshifts inaccuracies and failures

To determine the statistical distribution of spectroscopic redshifts, one needs to construct the probability distributions of  $z_p - z_s$  differences. Let  $p(z_s | z_p)$  denote the probability that a galaxy with the assigned photometric redshift  $z_p$  has the spectroscopic redshift  $z_s$ . The expected distribution of  $z_s$  is then a convolution of the photometric redshifts with the  $p(z_s | z_p)$  probability:

$$n(z_s) = \int dz_p p(z_s | z_p) n(z_p), \quad (11)$$

where  $n(z_p)$  is the observed distribution of the photometric redshifts. Since the distribution  $p(z_s | z_p)$  depends strongly on the galaxy magnitude, it is modelled separately in the consecutive magnitude bands. A thorough discussions of the  $z_s - z_p$  deviations (e.g. Ilbert et al. 2009; Dahlen et al. 2013) show that  $z_p$  errors are efficiently expressed using the parameter  $x = (z_p - z_s)/(1 + z_s)$ . It was found that a single Gaussian function adequately reproduces the probability distribution  $p(x)$  for the small absolute values of  $x$ , i.e. for the ‘successful’  $z_p$  estimates. But the  $p(x)$  has broad wings, inconsistent with the narrow central Gaussian peak, and for still larger  $x$  the probability distribution has small but quasi-constant amplitude.

The objective of our calculations is to assess the  $z_s$  distribution using the  $z_p$  data. It is natural to use in equation (11) somewhat different parametrization of the  $z_s - z_p$  differences, viz.  $y = (z_s - z_p)/(1 + z_p)$ . Since even at the fainter magnitudes the photometric redshifts provide statistically robust estimate of galaxy distances, the probability distributions  $p(y)$  and  $p(x)$  have similar construction. Consequently, function  $p(y)$  also exhibits narrow central peak, relatively wider wings and weak constant signal. To match these characteristics, we fit the analytic function that is a sum of three components: (a) the Gaussian – emulating the narrow peak near  $y \approx 0$ , (b) the resonance curve – to reproduce the contribution of larger  $z_p$  deviations and (c) the flat signal – reproducing the catastrophic errors. In total, six parameters of the  $p(y)$  distribution were determined. We applied the maximum likelihood (ML) estimation method. The detailed description of the fitted function and the whole procedure as well as the numerical results are presented in Appendix A.

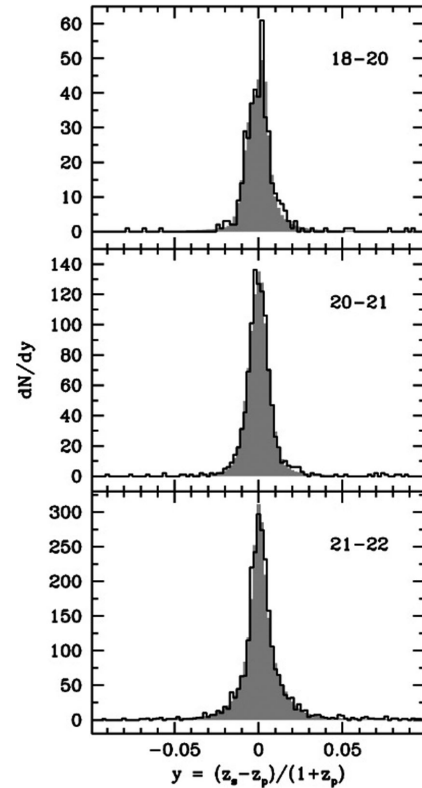


**Figure 6.** The distribution of  $z_s - z_p$  differences in three magnitude bands indicated in the upper right corners. Black line histogram – the observed distribution, the shaded area – the ML fit. The ordinate axis shows the number of galaxies with known spectroscopic redshifts.

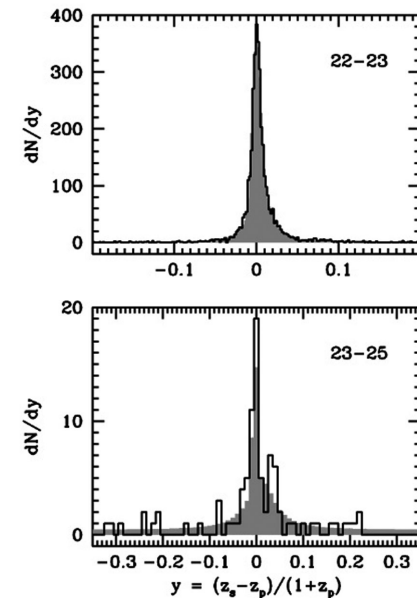


**Figure 7.** Same as Fig. 6 for magnitude bands 22 – 23 and 23 – 25.

The spectroscopic redshifts come mostly from zCOSMOS Data Release (Lilly et al. 2007). We searched also the NED Database, and several redshifts have been extracted from Onodera et al. (2012), Bezanson et al. (2013) and van de Sande et al. (2013). The fits are shown in Figs 6 and 7, where the ordinate axis gives the number of

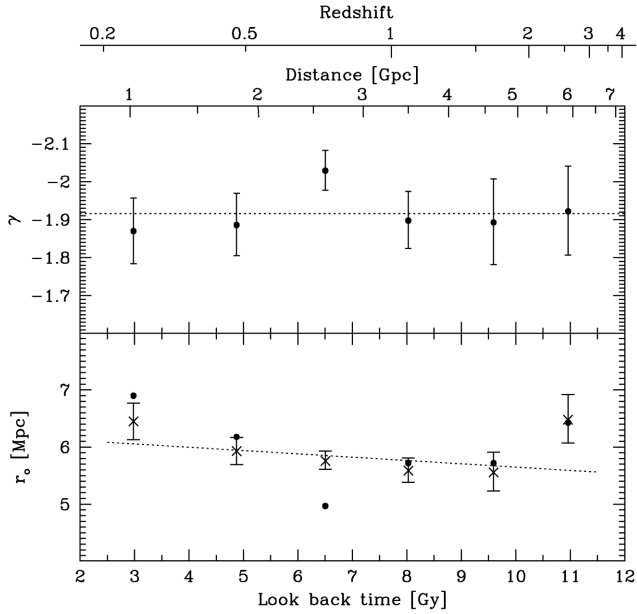


**Figure 8.** Power-law parameters:  $\gamma$  – slope, and  $r_0$  – normalization, of the spatial correlation function of class A galaxies versus look back time. Full dots show simultaneous fittings of  $\gamma$  and  $r_0$ ; crosses in the lower panel are the  $r_0$  best estimates assuming the slope fixed at the average value  $\gamma = -1.92$ .

objects rather than the probability. The galaxy sample was divided in 5 mag bins. In agreement with the Ilbert et al. (2009) discussion, the fits for galaxies brighter than 23 mag are strongly peaked at  $\gamma = 0$ , while the fainter objects exhibit substantially larger scatter. Nevertheless, despite a non-negligible number of ‘catastrophic’  $z_p - z_s$  discrepancies below 23 mag, the central concentration is still dominant. It allows us to use effectively equation (11). However, a relatively small number of the spectroscopic redshifts in the 23–25 mag bin generates the easily visible noise and broadens the uncertainty limits of the fitted parameters. This question is discussed in detail below.

#### 4.2 Correlation length

The spatial density of galaxies assigned to the  $i$ th distance class,  $\rho_i(R)$ , in equation (9) is related to the number of galaxies  $n_i(z_s)$  in a standard way:

$$\rho_i(R) = \frac{1}{\Omega R^2} \frac{dn_i(z_s)}{dR}, \quad (12)$$

where  $\Omega$  is the solid angle of the survey. Set of equations (9)–(12) allows us to determine the spatial density correlation parameter  $r_0$  for each distance bin. The galaxies in a given bin are spread over a range of magnitudes. Therefore, the probability distribution  $p(z_s | z_p)$  in equation (11) is weighted accordingly to the magnitude distribution of  $n_i(z_p)$  galaxies. Fig. 8 shows our best estimates of the CF parameters for class A galaxies. The error bars here are generated solely by uncertainties in the fitting of the power law to 2D CFs (Fig. 4). The errors represent 68 per cent uncertainties assuming one interesting parameter (Avni 1976).

A reasoning that photometric redshifts contain sufficient information to derive the amplitude of the space CF has been examined with positive results in the present investigation. Using extensive simulations, we generated the synthetic galaxy distribution of known space CF and then effectively determined the CF parameters according

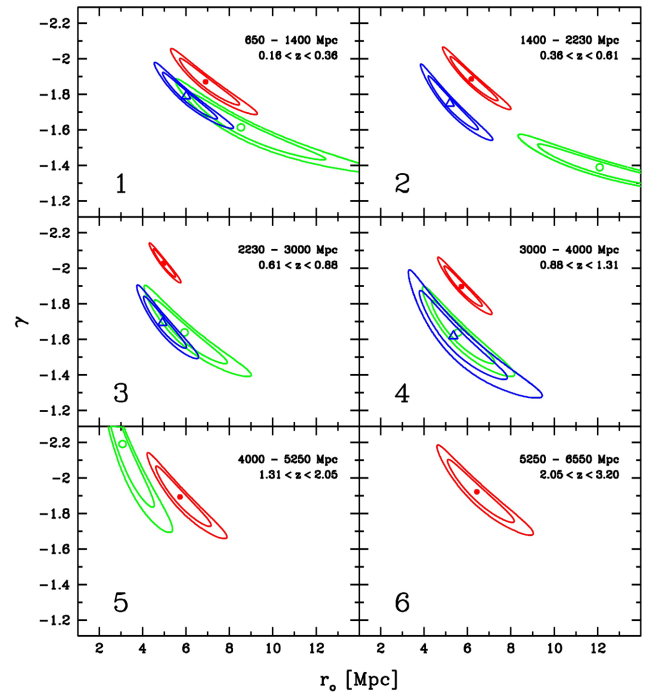


**Figure 9.** Power-law parameters of the correlation functions in the distance bins 1–6 (labelled in the bottom left corner); distance/redshift boundaries are indicated in the top right corner. Full dots – class A, open circles – class B, triangles – class C. Contours show regions of 68 and 90 per cent confidence level.

to the prescription presented above. The computational details are described in Appendix B.

The simultaneous fitting of  $\gamma$  and  $r_0$  induces strong correlation of both parameters.<sup>2</sup> In Fig. 9, the  $\gamma - r_0$  confidence regions are shown in all the distance bins for galaxies of class A; the data for the classes B and C are limited to 5 and 4 nearest bins, respectively. The contours do not incorporate uncertainties introduced by the estimates of the distribution of the  $z_s - z_p$  differences, or the ML fits of  $p(y)$ . To assess the  $p(y)$  uncertainties, the mock  $p(y)$  distributions were created using the bootstrap method. The details of the whole procedure are described in Appendix A.

We limited our analysis to the faintest galaxies because at the brighter magnitudes the  $p(y)$  distributions are based on an extensive data and the uncertainty of the  $p(y)$  fits is negligible. Small number of spectroscopic redshifts at faint magnitudes results in the poor quality of the  $p(y)$  fit in the  $23 < i^+ < 25$  band. The galaxies in the 23–25 mag dominate in the distance bins 4–6. They constitute 71, 97 and 99.5 per cent of the class A galaxies in the distance bins 4–6, respectively.

The calculations of  $r_0$  for the simulated  $p(y)$  probability functions were repeated as for the actual data. We find that the rms scatter of  $r_0$  produced by the uncertainties of the ML fitting amounts to 0.16, 0.26 and 0.29 Mpc for bins 4–6. Thus, the errors related to the ML fits are several times smaller than the uncertainties defined by the confidence level contours. Assuming that both errors add in

<sup>2</sup> To be precise, we fit simultaneously three parameters  $\eta_i$ ,  $w_i$  and  $\zeta_i$  of equation (4). Two of them are ‘interesting’, viz.  $w_i$  and  $\zeta_i$ . Observational correlation between  $w_i$  and  $\zeta_i$  is transferred into correlation between  $r_0$  and  $\gamma$  via equations (9) and (10).

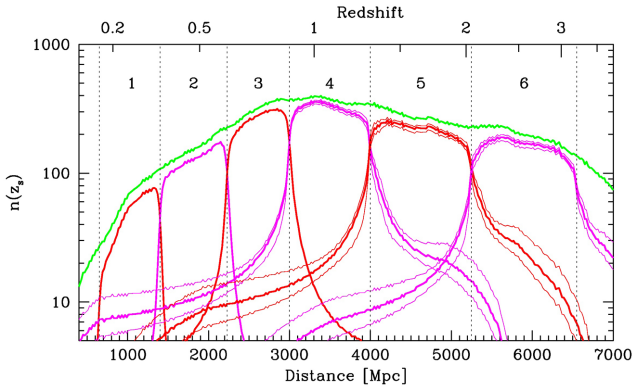


**Figure 10.** Thick curves – numbers of class A galaxies in six distance bins (indicated by labels 1–6) corrected for the  $z_p$  errors using equation (11). Thin curves –  $1\sigma$  uncertainty regions resulting from uncertainties of the  $z_s - z_p$  fits (see Appendix A for details.); shown only for three most distant bins where the errors are more pronounced. The upper envelope shows the summed galaxy numbers. The distance bins partially overlap because galaxies are assigned to their bins based on the photometric redshift.

squares, the uncertainties involved in the ML fitting do not contribute significantly to the total uncertainties.

#### 4.3 The radial extension of distance bins

In Fig. 10, we plot the radial distribution of the space density of galaxies luminosity class A calculated using equations (11) and (12). Although the effects of the photometric redshift errors are easily visible, the bins are still well defined in the real space. Long tails of the three most distant bins stretching towards the lower distances result from the catastrophic  $z_p$  errors.

It was shown in the previous section that the uncertainties of the  $p(y)$  fits contribute marginally to the total errors of our  $r_o$  estimates. This is because the  $p(y)$  scatter only weakly affects the  $n(z_p) \rightarrow n(z_s)$  transformation. The thin curves for three most distant bins in Fig. 10 show the rms uncertainty range of our  $n(z_s)$  reconstruction produced by the stochastic character of the  $p(y)$  estimates. It is visible that statistical uncertainties strongly affect only the low-amplitude tails of the individual  $n(z_s)$  distributions.

The composite shape of the  $\rho_i(R)$  distribution is accounted for in the calculations of the correlation length  $r_o$ . One should notice that the contribution to the  $r_o$  amplitude of the low-density extensions (that suffer from large uncertainties) is small as compared to the ‘central’ section of the bin. This is because the integral at the right-hand side of equation (9) contains the density square.

Relationships between the measured 2D CF and the 3D CF derived using equations (9) and (10) should be corrected for the finite radial extensions of bins. However, because the bin depths are substantially larger than the expected maximum separations at which the CF significantly deviates from zero, the effect is small as compared to statistical uncertainties. It was assessed as follows.

Counting galaxy pairs in the chosen distance bin corresponds to the double integration along the line of sight of the 3D CF weighted by the actual radial galaxy space density distribution. The difference between the results based on equation (7) and the pair number counts depends on the a priori unknown parameters of  $\xi(r)$ . Since this difference is expected to be small in the present calculation, we expressed the amplitude of the finite bin depth effect a posteriori, taking the best-fitting  $\xi(r)$  parameters as determined in the previous sub-section. In all the bins, the relative difference

between the analytic value used in equation (7) and the ‘effective’  $G$ -factor is negligible at the small separations, rises to  $\sim 1$  per cent at the transverse separations of 1–3 Mpc, and reaches 5–8 per cent (depending on the bin number) at  $\sim 20$  Mpc. The expected impact of this ‘integral constraint’ on the CF slope  $\gamma$  would be of the order of  $\sim 0.02$  with the correspondingly small effect for the correlation length.

## 5 DISCUSSION AND CONCLUSIONS

The mean absolute magnitude of galaxies in the sample A coincides roughly with the characteristic magnitude  $M^*$  in the Schechter luminosity function. Because of the flux selection, the mean magnitude difference between the samples A–C varies with the distance. In the first three distance bins, galaxies in the sample B are fainter than class A galaxies by  $\sim 1.4$  mag, while in the distance bins 4 and 5 this difference drops to 1.3 and 1.2, respectively. The magnitude separation between sample A and C is more strongly affected by the selection. It amounts to 2.9 mag in the first two distance bins, and is reduced to 2.7 and 2.3 in the next two bins, respectively.

A comparison of our CF slope estimates with a number of fragmentary measurements present in the literature leads to somewhat ambiguous conclusions. Marulli et al. (2013) compile a number of recent results on the CF parameters derived for a wide range of galaxy luminosities and redshifts. Our results fit well to the general distribution of measurements in their fig. 5. In particular, the slope flattening in the sample B and C as compared to the sample A seems to be present also in the published results (e.g. Pollo et al. 2006; Coil et al. 2006). One should note, however, that individual measurements refer frequently to different redshifts and are subject to large uncertainties. Therefore, questions on the specific relationships between CF parameters still remain open. The VIPERS data (Marulli et al. 2013) that suffer from the smallest uncertainties, indicate a weak but systematic flattening of the slope with redshift, while this effect is not indicated by our investigation. Furthermore, these data show only a marginal CF slope – absolute magnitude dependence. One should note, however, that the VIPERS galaxies in the Marulli et al. (2013) data span a relatively narrow magnitude range of  $\Delta M \approx 1.5$ , and are confined to redshifts between 0.5 and 1.1.

Despite considerable size of the banana shape confidence regions in Fig. 9, our estimates of  $\gamma$  and  $r_o$  provide constraining information on the cosmic evolution of the galaxy CF. Although, the relative positions of the best-fitting parameters in the  $r_o$ – $\gamma$  plane of class A–C galaxies vary from one distance bin to the another, the shape and orientation of the confidence regions demonstrate some permanent characteristics of the CF over a wide redshift range. It appears that the correlation length,  $r_o$ , of class A–C galaxies is quite similar in most of the distance bins, although not necessarily identical. Larger discrepancies between class B and A in the distance bin 2 and 5 are of the opposite sign, and seem to be generated by statistical fluctuation in the data rather than the cosmic signal. The conclusion in the previous section that the CF slope is steeper for the most luminous galaxies (class A) is strengthened by the overall layout of the confidence regions.

Marulli et al. (2013) reach the opposite conclusion. They find ‘a monotonic increase in the clustering length  $r_o$ ’ as a function of magnitude ‘in all three redshift ranges considered’, i.e. 0.5–0.7, 0.7–0.9 and 0.9–1, 1. Taking into account elongated shapes of the confidence regions, such interpretation of Fig. 9 is not completely ruled out; however, it is not favoured by the present results.

It is instructive to compare our results with the Arnalte-Mur et al. (2014) investigation, as it also uses photometric redshifts, and covers a relatively wide redshift range,  $0.35 < z < 1.25$ . Their fig. 7 apparently indicates a rise of the correlation length with galaxy luminosities, but no obvious dependence of the correlation slope on the luminosities. Despite these differences, both investigations support the conclusion that the clustering amplitude increases with the galaxy luminosities. Our Fig. 9 shows that the present calculations are not immune to statistical fluctuations. The question of systematic errors is more ambiguous. It is assumed in the present method that all the known as well as unrecognized selection effects that alter the galaxy distribution are accounted for using the information incorporated in the catalogue itself. In the alternative methods, the mock catalogues are used as a reference ‘random’ distribution. Such catalogues are designed to model all the instrumental/observational constraints that modify the genuine galaxy clustering. A question which of these two methods is more suitable for dealing with various observational biases depends on the particular properties of the observational data. The overall characteristics of the COSMOS/Subaru catalogue, namely very wide redshift coverage of relatively small surface area with numerous gaps, favour the method developed in this paper.

Because of the apparently constant slope of the CF for the class A galaxies, it is reasonable to fix the slope for all the bins at the average value of  $\bar{\gamma} = -1.92$ . The best estimates of  $r_0$  in this case are shown with crosses in the lower panel of Fig. 8. There is a weak indication that  $r_0$  slowly increases with the cosmic time. The dotted line in the lower panel shows the least-squares linear fit to the  $r_0$  versus look back time. The slope of this line differs from 0 at  $1.14 \sigma$ .

The issue whether the present results are representative for the general galaxy clustering properties or refer just to the COSMOS field cannot be answered using this field alone. The question is legitimate because of some peculiarities in the field were reported in the literature (e.g. Meneux et al. 2009). We would postpone the answering to this until the similar analysis is performed on other deep fields.

### 5.1 The bias

The homogeneous computation scheme applied to the galaxies spread over a huge redshift range allowed us for a uniform assessment of the clustering evolution as well as the galaxy bias,  $b(z)$ :

$$b(z) = \sigma_g(z)/\sigma_m(z), \quad (13)$$

where  $\sigma_g(z)$  denotes the galaxy number rms fluctuations and  $\sigma_m(z)$  the mass rms fluctuations within the same volume. The CF is rigorously connected to the galaxy rms fluctuations. In particular, the rms of the galaxy number in a sphere of radius  $r$  is related to the power-law CF (Peebles & Groth 1976):

$$\sigma_g(r|z) = [C_\gamma \xi(r|z)]^{1/2}, \quad (14)$$

where  $C_\gamma = 72 \cdot 2^\gamma / [(3 + \gamma)(4 + \gamma)(6 + \gamma)]$ , and the volume size as well as the redshift dependence of  $\sigma$  and  $\xi$  are explicitly indicated. The growth of the matter fluctuations,  $\sigma_m(r|z)$ , in the linear regime is completely defined by the cosmological model. In the following, we use the set of equations listed by Meneux et al. (2008):  $\sigma_m(r|z) = \sigma_m(r|0)/D(z)$ , where  $D(z) = g(z)/[g(0)(1+z)]$  and  $g(z) = \frac{5}{2} \Omega_m / [\Omega_m^{4/7} - \Omega_\Lambda + (1 + \Omega_m/2)(1 + \Omega_\Lambda/70)]$  is the normalized growth factor (Carroll, Press & Turner 1992). The evolving

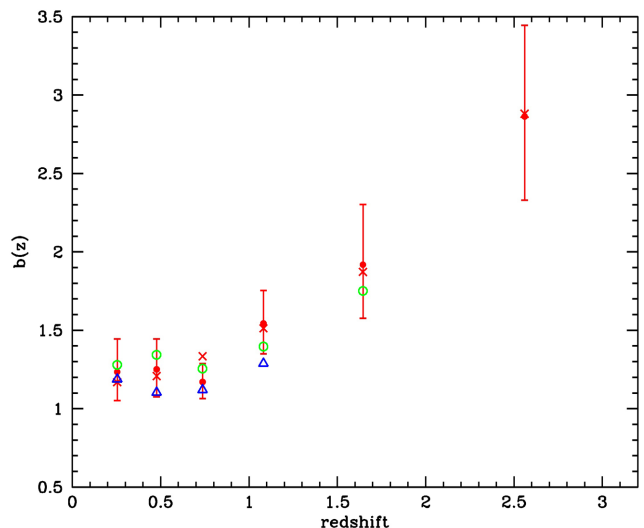


**Figure 11.** The redshift evolution of the linear bias factor. Dots denote the bias factor calculated for the  $r_0$  and  $\gamma$  fits of class A galaxies indicated with dots in Fig. 8. The error bars correspond to 68 per cent uncertainties drawn in Fig. 9. Crosses show the bias of the class A galaxies assuming the slope of the correlation function fixed at  $\gamma = -1.92$  (crosses in Fig. 8). The bias factor for B and C classes are shown with open circles and triangles, respectively.

density parameters  $\Omega_m$  and  $\Omega_\Lambda$  are related to their present epoch values:

$$\Omega_m \equiv \Omega_m(z) = \frac{\Omega_{m,0}(1+z)^3}{E^2(z)}, \quad \Omega_\Lambda \equiv \Omega_\Lambda(z) = \frac{\Omega_{\Lambda,0}}{E^2(z)}, \quad (15)$$

where  $E^2(z) = \Omega_{\Lambda,0} + \Omega_{m,0}(1+z)^3$  is the expansion factor for the flat cosmological model, for which  $\Omega_\Lambda + \Omega_m = 1$ . The present epoch mass fluctuations amplitude,  $\sigma_m(0)$ , is commonly normalized to the mass rms within a sphere of radius  $r = 8 h^{-1}$  Mpc, where  $h = H_0/100 \text{ km s}^{-1} \text{ Mpc}^{-1}$ . We use the Komatsu et al. (2011) figure  $\sigma_m(0) = 0.82$  based on 7 yr WMAP observations. The bias–redshift relations deduced from the CF measurements are shown in Fig. 11. Dots and crosses indicate the bias variations of the class A galaxies, circles – class B, and triangles – class C. Growth of  $b(z)$  for the most luminous (class A) galaxies reported in the literature for low and moderate redshifts (e.g. Marinoni et al. 2005; Papageorgiou et al. 2012) continues to high redshifts. The data for galaxies class B and C are limited to low redshifts and apparently the bias amplitude does not depend on the galaxy luminosities in that area. It is difficult to assess whether the bias coincidence at low redshift of the class A–C galaxies contradicts the well documented relationship between the bias and galaxy luminosities. This is because a sharp rise of the bias amplitude with galaxy luminosities (e.g. Zehavi et al. 2011) is mostly constrained to galaxies brighter than  $M^*$ , while our class A corresponds roughly to  $M^*$ , and classes B and C are fainter.

In low and moderate redshifts, the present results are largely consistent with the measurements based on the galaxy samples with spectroscopic redshifts. The photometric redshifts provide only the statistical constraints on the galaxy distribution, and cannot be used to localize precisely individual objects. This inevitably broadens the uncertainties of our estimates. However, the photometric redshifts can be determined in massive scale over much larger volume of the Universe than it is now feasible for the spectroscopic surveys. The present calculations are based purely on the observational data, i.e. in the calculations we do not include mock galaxy catalogues conceived from the cosmological simulations. This

additionally increases our final uncertainties. However, our method is more adequate as long as effects of the cosmic variance on the galaxy clustering are not fully accounted for.

Our high-redshift measurements of the galaxy linear bias fit well in the low-redshift limit to the previous studies. To assess more precisely the evolution trends of the galaxy CF at high redshifts, we plan to perform analogous investigation on other deep galaxy photometric redshift surveys.

## ACKNOWLEDGEMENTS

We thank the anonymous reviewer for her recommendations that greatly helped us to improve the presentation of our analysis. Based on zCOSMOS observations carried out using the Very Large Telescope at the ESO Paranal Observatory under Programme ID: LP175.A-0839. This work has been partially supported by the Polish NCN grant 2011/01/B/ST9/06023.

## REFERENCES

- Arnalte-Mur P., Martínez V. J., Norberg P., Fernández-Soto A., Ascaso B., Merson A. I., Aguerri J. A. L., Castander F. J., 2014, *MNRAS*, 441, 1783
- Arnouts S., Ilbert O., 2011, LePHARE: Photometric Analysis for Redshift Estimate, Astrophysics Source Code Library
- Avni Y., 1976, *ApJ*, 210, 642
- Baugh C. M., 1996, *MNRAS*, 280, 267
- Berlind A. A., Weinberg D. H., 2002, *ApJ*, 575, 587
- Bezanson R., van Dokkum P., van de Sande J., Franx M., Kriek M., 2013, *ApJ*, 764, L8
- Bielby R. M., Gonzalez-Perez V., McCracken H. J., Ilbert O., Daddi E., Le Fèvre O., Hudelot P., Kneib J.-P., 2014, *A&A*, 568, A24
- Carroll S. M., Press W. H., Turner E. L., 1992, *ARA&A*, 30, 499
- Coil A. L., Newman J. A., Cooper M. C., Davis M., Faber S. M., Koo D. C., Willmer C. N. A., 2006, *ApJ*, 644, 671
- Coupon J. et al., 2012, *A&A*, 542, A5
- Dahlen T., Mobasher B., Faber S. M., Ferguson H. C., Barro G., Finkelstein S. L., Finlator K., Fontana A., 2013, *ApJ*, 775, 93
- Fry J. N., 1996, *ApJ*, 461, L65
- Heinis S., Milliard B., Arnouts S., Blaizot J., Schiminovich D., Budavári T., Ilbert O., Donas J., 2007, *ApJS*, 173, 503
- Huterer D., Kirkby D., Bean R., Connolly A., Dawson K., Dodelson S., Evrard A., Jain B., 2015, *Astropart. Phys.*, 63, 23
- Ilbert O., Capak P., Salvato M., Aussel H., McCracken H. J., Sanders D. B., Scoville N., Kartaltepe J., 2009, *ApJ*, 690, 1236
- Jenkins A. et al., 1998, *ApJ*, 499, 20
- Jennings E., Baugh C. M., Pascoli S., 2011, *ApJ*, 727, L9
- Kaiser N., 1984, *ApJ*, 284, L9
- Komatsu E., Smith K. M., Dunkley J., Bennett C. L., Gold B., Hinshaw G., Jarosik N., Larson D., 2011, *ApJS*, 192, 18
- Li C., Kauffmann G., Jing Y. P., White S. D. M., Börner G., Cheng F. Z., 2006, *MNRAS*, 368, 21
- Lilly S. J., Le Fèvre O., Renzini A., Zamorani G., Scodreggio M., Contini T., Carollo C. M., Hasinger G., 2007, *ApJS*, 172, 70
- Lin L. et al., 2012, *ApJ*, 756, 71
- McCracken H. J., Ilbert O., Mellier Y., Bertin E., Guzzo L., Arnouts S., Le Fèvre O., Zamorani G., 2008, *A&A*, 479, 321
- Marinoni C., Le Fèvre O., Meneux B., Iovino A., Pollo A., Ilbert O., Zamorani G., Guzzo L., 2005, *A&A*, 442, 801
- Martinez-Manso J., Gonzalez A. H., Ashby M. L. N., Stanford S. A., Brodwin M., Holder G. P., Stern D., 2015, *MNRAS*, 446, 169
- Marulli F., Bolzonella M., Branchini E., Davidzon I., de la Torre S., Granett B. R., Guzzo L., Iovino A., 2013, *A&A*, 557, A17
- Meneux B., Guzzo L., Garilli B., Le Fèvre O., Pollo A., Blaizot J., De Lucia G., Bolzonella M., 2008, *A&A*, 478, 299
- Meneux B., Guzzo L., de la Torre S., Porciani C., Zamorani G., Abbas U., Bolzonella M., Garilli B., 2009, *A&A*, 505, 463

- Mo H. J., White S. D. M., 1996, *MNRAS*, 282, 347
- Mostek N., Coil A. L., Cooper M., Davis M., Newman J. A., Weiner B. J., 2013, *ApJ*, 767, 89
- Norberg P., Baugh C. M., Hawkins E., Maddox S., Madgwick D., Lahav O., Cole S., Frenk C. S., 2002, *MNRAS*, 332, 827
- Onodera M., Renzini A., Carollo M., Cappellari M., Mancini C., Strazzullo V., Daddi E., Arimoto N., 2012, *ApJ*, 755, 26
- Papageorgiou A., Plionis M., Basilakos S., Ragone-Figueroa C., 2012, *MNRAS*, 422, 106
- Peebles P. J. E., Groth E. J., 1976, *A&A*, 53, 131
- Pollo A., Guzzo L., Le Fèvre O., Meneux B., Cappi A., Franzetti P., Iovino A., McCracken H. J., 2006, *A&A*, 451, 409
- Taniguchi Y., Scoville N., Murayama T., Sanders D. B., Mobasher B., Aussel H., Capak P., Ajiki M., 2007, *ApJS*, 172, 9
- Totsuji H., Kihara T., 1969, *PASJ*, 21, 221
- van de Sande J. et al., 2013, *ApJ*, 771, 85
- Wake D. A. et al., 2011, *ApJ*, 728, 46
- Zehavi I., Zheng Z., Weinberg D. H., Blanton M. R., Bahcall N. A., Berlind A. A., Brinkmann J., Frieman J. A., 2011, *ApJ*, 736, 59

## APPENDIX A: ANALYTIC FITS OF THE $z_p - z_s$ DEVIATIONS

Distribution of  $z_p - z_s$  differences is represented using the probability distribution  $p(y)$ , where  $y = (z_s - z_p)/(1 + z_p)$ .

Complex nature of the  $z_p - z_s$  deviations requires adequate functional form that accounts for a high fraction of almost perfect  $z_p$  measurements as well as casual errors and sporadic failures. Accordingly, the  $p(y)$  distribution is defined as the normalized sum of three components: the Gaussian function  $g(y)$ , the resonance function  $r(y)$  and a low-amplitude uniform probability  $\alpha_0$ :

$$p(y) = \alpha_g \cdot g(y) + \alpha_r \cdot r(y) + \alpha_0, \quad (\text{A1})$$

where

$$g(y) = \frac{1}{\sqrt{2\pi}s_g} \exp[-(y - \mu_g)^2/2s_g^2] \quad (\text{A2})$$

$$r(y) = \frac{1}{\pi} \frac{s_r}{(y - \mu_r)^2 + s_r^2},$$

Parameters  $\mu_g$ ,  $s_g$ ,  $\mu_r$  and  $s_r$  plus relative contributions of the components,  $\alpha_g$ ,  $\alpha_r$  and  $\alpha_0$  are fitted to the observed distributions of the  $y$  parameter. The ML estimation was applied. Since the quality of the photometric redshifts deteriorates with increasing magnitude, the data were divided into 5 mag bands. A small number of measured spectroscopic redshifts below  $m = 23$  and a high fraction of  $z_p$  catastrophic errors potentially could introduce relatively large uncertainties to the present analysis. The question to what extent uncertainties related to the fitting procedure affect our estimates of the space correlation amplitude is addressed as follows.

We generated 200 quasi-random samples of the  $(z_s, z_p)$  pairs using the bootstrap method. The mock samples were drawn from the real data. The average amplitudes of parameters fitted to the simulations and their rms scatter have been calculated. The results of the entire procedure are listed in Table A1. The first five rows give the best-fitting parameters to the real data while the bottom two rows show the results for the simulated 23–25 mag bin.

Because of the distinctive form of the fitted function the parameters are strongly correlated. Therefore the resultant  $p(y)$  distributions exhibit a moderate variations, despite the high scatter of individual parameters. Stable character of  $p(y)$  distribution generates via equation (11) well-defined spectroscopic redshift distributions,  $n(z_s)$ . We assessed the uncertainties of  $n(z_s)$  from a spread of the mock distributions. A set of 200 simulated spectroscopic redshift data,  $n(z_s)$ , was generated using the simulated  $p(y)$  probability

**Table A1.** Parameters for the  $p(y)$  distributions in 5 mag bins.

Mag bin	$N_s^a$	$\alpha_o$	$\alpha_g$	$\mu_g$	$s_g$	$\alpha_r$	$\mu_r$	$s_r$
18.0–20.0	407	0.0028	0.3368	−0.0045	0.0042	0.6604	0.0028	0.0039
20.0–21.0	1050	0.0085	0.5423	−0.0006	0.0059	0.4492	0.0009	0.0049
21.0–22.0	2521	0.0120	0.1942	0.0037	0.0110	0.7938	0.0004	0.0045
22.0–23.0	3775	0.0239	0.3300	−0.0008	0.0044	0.6461	0.0039	0.0094
23.0–25.0	89	0.1773	0.1886	−0.0034	0.0026	0.6341	0.0042	0.0298
Simulations								
23.0–25.0	Average	0.2090	0.2482	−0.0037	0.0036	0.5428	0.0096	0.0256
	rms	0.0968	0.1110	0.0015	0.0033	0.1710	0.0132	0.0138

Note.<sup>a</sup> Number of galaxies with measured spectroscopic redshifts used in the fittings.

functions. The rms scatter of  $n(z)$  is indicated in Fig. 10 with thin curves for three most distant bins.

## APPENDIX B: TESTING THE ESTIMATORS OF CF PARAMETERS

The full procedure of measuring the 3D CF parameters using the catalogue of photometric redshifts has been tested on the simulated data. First, we generate a 3D point distribution according to a priori defined statistical characteristics. Then, the data are processed in the same way as the COSMOS observations to retrieve the CF parameters. Finally, the results are confronted with the original values.

### B1 Modelling the space distribution with definite CF

The objective was to construct the model distribution of points characterized by the power-law CF with the slope and normalization close to those determined for the COSMOS data. This synthetic material was not devised to imitate other statistical properties of the real galaxy population. From among a diversity of space distributions satisfying the selected CF, we took a computationally manageable position-dependent function. The particular point distribution was realized by the MC method. The points were drawn according to the properly defined probability distribution. The algorithm that provided an acceptable approximation for the power-law CF was constructed as follows.

Two populations of points are distributed within a specified volume: (a) points concentrated in ‘clusters’,<sup>3</sup> and (b) ‘field’ points distributed randomly, but outside clusters. The cluster centres are distributed fully randomly. Points within each cluster are distributed according to the broken power law:

$$\rho(r) = \begin{cases} \rho_b \left(\frac{r_1}{r_2}\right)^{\alpha_2} \left(\frac{r}{r_1}\right)^{\alpha_1} & \text{for } r < r_1 \\ \rho_b \left(\frac{r}{r_2}\right)^{\alpha_2} & \text{for } r_1 \leq r < r_2 \\ \rho_b & \text{for } r \geq r_2, \end{cases} \quad (\text{B1})$$

where  $\rho_b$  is the space density of points outside clusters,  $r_1$  and  $r_2$  are characteristic cluster radii that delineate two zones of distinct power indices  $\alpha_1$  and  $\alpha_2$ . The amplitude of the CF depends also on the number of clusters or equivalently – on the fraction of volume occupied by clusters. In the subsequent calculations, we adopted the following parameter values: radii  $r_1$  and  $r_2$  of 6 and 16 Mpc, respectively, and the power-law indices  $\alpha_1 = -2.44$  and  $\alpha_2 = -1.25$  for the central and outer cluster zones. The volume occupied by

<sup>3</sup> Here, ‘clusters’ represent clumps of points that generate the required CF, with no relation to the real galaxy clusters.

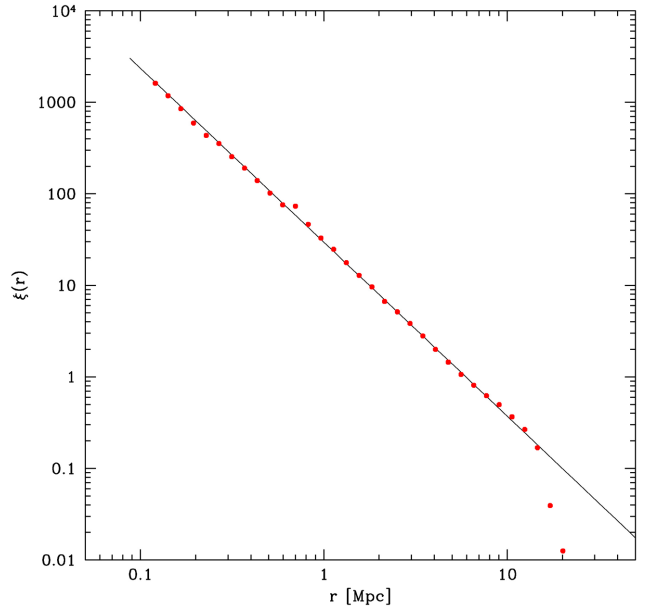


**Figure B1.** Dots – the correlation function of 62 158 points distributed according to the model described in the text, line – the power-law fit  $\xi(r) = (r/r_m)^{\gamma_m}$  with  $r_m = 5.89$  Mpc and  $\gamma_m = -1.89$ .

clusters was selected at  $\kappa \approx 0.40$  of the total survey volume. This set of parameters determines the relative contribution of field and clustered points to the total number at 0.33 and 0.67, respectively.

The present prescription of the space point distribution yields the CF emulating the power law over a wide range of separations extending up to  $\sim 15$  Mpc. This is illustrated in Fig. B1, where  $\sim 62\,000$  points were distributed in a volume of  $1.73 \times 10^7$  Mpc<sup>3</sup> according to equation (B1) with  $\rho_b = 2.25 \times 10^{-3}$  Mpc<sup>-3</sup>. Fitting the power law to the CF generated by this set of parameters gives the slope  $\gamma_m = -1.9$  and the correlation length  $r_m = 5.9$  Mpc.

It is important to emphasize that this model distribution generates the definite CF but has no resemblance to the actual galaxy space distribution. The objective of the procedure is just to test the efficiency of the method, i.e. whether the algorithm presented in Sections 3 and 4 is able to extract the parameters of the CF from the surface data. One can expect that individual realizations of the synthetic model limited to the volume of the COSMOS field would provide the CF parameters scattered around the original values assumed in the simulations. The size of this spread is characteristic to the model and does not represent uncertainties of the CF parameters derived from the real data.

**Table B1.** Parameter estimation applied to the simulated, synthetic catalogues of photometric redshifts.

Distance bin	No mask		BS		BS + $F_{0.025}$		BS + $F_{0.05}$		BS + $F_{0.10}$		rms	
	$\gamma$	$r_o$	$\gamma$	$r_o$	$\gamma$	$r_o$	$\gamma$	$r_o$	$\gamma$	$r_o$	$\gamma$	$r_o$
1	-1.87	6.6	-1.87	6.5	-1.89	6.3	-1.84	6.8	-1.88	6.4	0.22	2.2
2	-1.87	6.1	-1.86	6.3	-1.87	6.1	-1.87	6.2	-1.87	6.2	0.10	1.1
3	-1.88	6.1	-1.87	6.1	-1.88	6.1	-1.88	6.1	-1.87	6.1	0.11	0.9
4	-1.86	6.3	-1.86	6.3	-1.87	6.3	-1.88	6.2	-1.86	6.3	0.09	0.9
5	-1.87	6.0	-1.90	5.8	-1.88	5.9	-1.89	5.9	-1.90	5.9	0.15	1.1
6	-1.88	6.2	-1.91	6.1	-1.90	6.1	-1.90	6.1	-1.89	6.2	0.21	1.6

*Notes.* The simulated data points were drawn according to the underlying probability distribution that generates the power-law CF with  $\gamma = -1.89$  and  $r_o = 5.9$  Mpc. BS – bright star mask,  $F_{0.025}$ ,  $F_{0.05}$ , and  $F_{0.10}$  – filters; see text for details.

## B2 Extracting the PL parameters from the model data distributed in the COSMOS field

We now adjust our model to the global constraints that shape the COSMOS data. The objective is to reproduce some basic statistical characteristics (such as the total number of objects and a form of the radial distribution) of the most luminous galaxies, denoted as class A.

First, the points are distributed in a pyramid volume of the solid angle of  $1.42 \times 1.38 \text{ deg}^2$ , what corresponds to the size of the COSMOS/Subaru field. To emulate a decreasing space density of galaxies at large distances, the probability of qualifying a point for further processing was adequately reduced. In effect, the final set of ‘objects’ contained  $\sim 76\,000$  points. We declare that the present method is essentially insensitive to the numerous empty regions distributed over the field as well as to the smooth, large angular scale inhomogeneities of the survey. Although variations of the limiting magnitudes have been investigated (Taniguchi et al. 2007), and the final catalogue is free from substantial inhomogeneities, one should allow for some residual instrumental fluctuations that simulate the clustering signal. To check that, we ran the tests with a superimposed mask that imitates holes in the actual catalogue due to the bright stars. The ‘Swiss cheese’ mask contains above 125 circles representing the most prominent blank fields. Additionally, we test the effects of potential angular inhomogeneities of the survey. This is achieved by applying the ‘fluctuation filter’,  $F_a$ . We superimpose a filter that introduces fluctuations of the point surface density with a characteristic wavelength  $\lambda = 40$  arcmin in both directions (RA and Dec.):

$$n(x, y) = \bar{n} [1 + a \sin(kx) \sin(ky)], \quad (\text{B2})$$

where  $n(x, y)$  and  $\bar{n}$  are the local and the mean point densities, respectively,  $a$  is the fluctuation amplitude, and  $k = 2\pi/40$  arcmin. Three amplitudes  $a$  were applied: 0.025, 0.05 and 0.10

‘Spectroscopic redshifts’ were assigned to all the objects assuming the cosmological model adopted in the paper. To attach a ‘photometric redshift’ to each object, we apply a method identical to that described in Appendix A. Using the ML method, we find the best-fitting parameters of the  $p(x)$  probability distribution, where  $x = (z_p - z_s)/(1 + z_s)$ . Since the overall shape of  $p(x)$  and  $p(y)$  is similar, the functional form of both distribution is the same. The COSMOS  $p(x)$  distributions depend on the apparent magnitude of objects. To mimic this effect, each object in our catalogue was labelled with the ‘apparent magnitude’ drawn from the magnitude distribution of the real data.

The final simulated catalogue contained the list of points identified just by their angular coordinates and photometric redshifts. Such ‘observational material’ was analysed using the method and formulae in Sections 3 and 4. Calculations were performed for 25

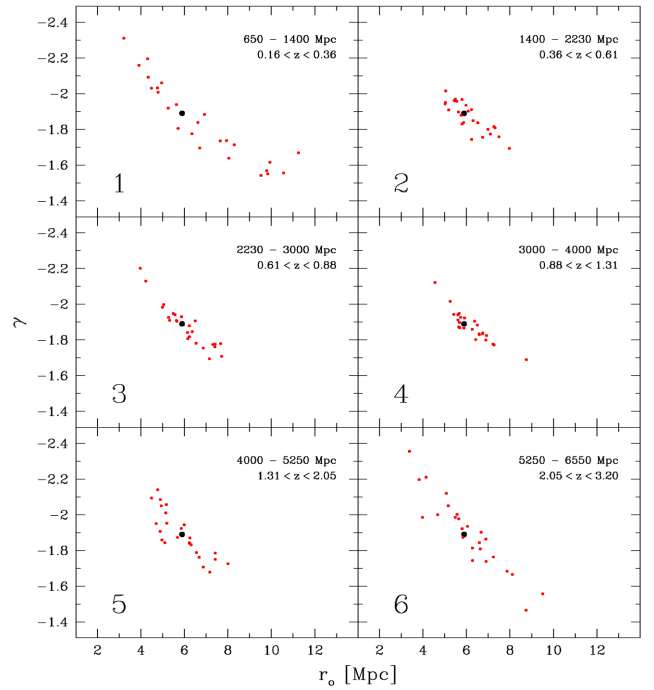


**Figure B2.** Estimates of the power-law parameters of the correlation functions for 25 sets of simulated data with the ‘bright star’ mask and ‘fluctuation filter’  $F_{0.05}$ . The input CF parameters are indicated by large full dots; parameters extracted using the present method are shown with small dots. See text for details.

sets of simulated catalogues, using various combinations of the bright star mask (BS) and fluctuation filters ( $F_{0.025}$ ,  $F_{0.05}$  and  $F_{0.10}$ ). The quantitative comparison of the CF parameter estimates,  $\gamma$  and  $r_o$ , with their model amplitudes of  $-1.89$  and  $5.89$  Mpc is summarized in Table B1. In columns 2–11, the average amplitudes for  $\gamma$  and  $r_o$  of 25 data sets are shown. In the last two columns, the rms scatter averaged over all the mask + filter settings is given.

We note that, in fact, the mask and filters do not introduce any systematic corrections to our estimates of the CF parameters. One could expect a moderate raise of uncertainties because both modifications add an additional noise to the data. However, the effect is small and the total scatter is dominated by the stochastic nature of the simulated catalogues. In Fig. B2, the distributions of 25 runs with the BS mask and the fluctuation filter  $F_{0.05}$  are shown in the  $r_o$ – $\gamma$  plane. It appears that the distributions of both parameters are roughly centred on their original amplitudes. Although, some bias towards flatter slopes and larger correlation length is visible in distance bins that contain lower number of objects.

One should notice that the extent of the scatter plots in Fig. B2 results from the statistical character of the investigated matter. That includes also particular distribution of clusters in the simulated catalogues. Therefore, the parameter dispersion derived for the synthetic catalogues is a sum of two components. First, it is generated by the noise associated with the drawing of points according to the specific underlying probability distribution. Second, it results from the different realizations of probability distribution itself. Thus, the scatter plots in Fig. B2 do not represent the uncertainties of parameters estimated from the real data.

A good agreement between the input parameters and their estimates indicates that the procedures introduced in the paper can be used to derive the space characteristics of the CF using photometric redshifts. Possible systematic deviations, if any, are substantially smaller than large statistical uncertainties.

This paper has been typeset from a  $\text{\TeX}/\text{\LaTeX}$  file prepared by the author.